PAPER

Check for updates

Assessment and control of the impermeability of graphene for atomically thin membranes and barriers†

Piran R. Kidambi, [ID] *[a,c] Rebekah A. Terry,[a] Luda Wang,[a] Michael S. H. Boutilier,[a] Doojoon Jang,[a] Jing Kong[b] and Rohit Karnik [ID] *[a]

Two-dimensional materials such as graphene offer fundamentally transformative opportunities in membrane separations and as impermeable barriers, but the lack of facile methods to assess and control its 'impermeability' critically limits progress. Here we show that a simple etch of the growth catalyst (Cu) through defects in monolayer graphene synthesized by chemical vapor deposition (CVD) can be used to effectively assess graphene quality for membrane/barrier applications. Using feedback from the method to tune synthesis, we realize graphene with nearly no nanometer-scale defects as assessed by diffusion measurements, in contrast to commercially available graphene that is largely optimized for electronic applications. Interestingly, we observe clear evidence of leakage through larger defects associated with wrinkles in graphene, which are selectively sealed to realize centimeter-scale atomically thin barriers exhibiting <2% mass transport compared to the graphene support. Our work provides a facile method to assess and control the 'impermeability' of graphene and shows that future work should be directed towards the control of leakage associated with wrinkles.

Introduction

Atomically thin (2D) materials such as graphene have recently attracted significant research interest as ultrathin barriers for mass transport[1–3] and as gas/liquid separation membranes for materials/chemical processing, sensing, fuel cells, desalination, carbon capture and storage and dialysis.[4–8,51] Graphene exhibits a theoretical minimum material thickness of ~0.34 nm, which, combined with chemical resistance, high mechanical strength (~42 N m^{-1}, 130 GPa), Young's modulus (~1 TPa) and the ability to sustain nanometer sized pores, offers the possibility of creating new kinds of membrane with transformative improvements in permeance, selectivity and robustness.[9,10] The space between the six sp^2 bonded carbon atoms in the hexagonal graphene lattice is too small for transport of even the smallest of gas molecules such as He (van der

Waals radius ~0.28 nm) or H$_2$ (~0.314 nm), thereby making graphene an ideal barrier material.[1–3] Experimental observations have shown that pristine flakes of graphene, exfoliated from graphite, are indeed impermeable to He but allow transport of protons.[1,3] However, exfoliation is inherently unsuitable for membrane and barrier applications that require large-area synthesis.

While several methods for the synthesis of 2D materials exist, chemical vapor deposition (CVD) has emerged as one of the most preferable routes for scalable, cost effective, high-quality material synthesis.[11–13] However, to this date the quality of CVD graphene and other 2D materials has largely been optimized for electronic applications.[14–16] The quality requirements for membrane and mass transport barrier applications tend to be different, and significantly more stringent in some respects. For example, sparse multiple-atom vacancy defects may significantly compromise the barrier properties of graphene (by leakages that heavily compromise selectivity), but may remain un-detected in most electronic applications. Although CVD graphene is inherently polycrystalline, with grain boundaries[17,18] that are detrimental for charge transport in electronic applications,[19–21] little is known about the origin, aggregation and subsequent manifestation of defects with regard to membrane and barrier applications.[22–24] The large parameter space[11] in the synthesis of CVD graphene, the lack of a suitable quality metric for "membrane/barrier quality

[a]Department of Mechanical Engineering, Massachusetts Institute of Technology, Cambridge, MA 02139, USA. E-mail: krpiran@mit.edu, karnik@mit.edu
[b]Department of Electrical Engineering and Computer Science and Research Laboratory of Electronics, Massachusetts Institute of Technology, Cambridge, MA 02139, USA
[c]Department of Chemical and Biomolecular Engineering, Vanderbilt University, Nashville, TN 37240, USA

graphene" (*i.e.* the lack of a simple technique to probe nanometer sized pores over a large area), and few studies using large area membranes/barriers have acutely limited its progress in this field.[5–8,16,25–33]

Here, we report on the quantitative investigation and development of a simple, cost effective and rapid characterization technique based on a facile etch of the growth catalyst (Cu) to assess the quality of CVD graphene for membrane and barrier applications. Using this simple technique, we rapidly screened the parameters for CVD synthesis of graphene and converged on optimum synthesis conditions for "barrier/membrane quality graphene" that is devoid of sub-nanometer to nanometer-scale defects, except at wrinkles. Finally, we showed that the etch test can account for experimentally measured transport properties of graphene membranes, and that defects at wrinkles can be sealed to obtain centimeter-scale single-layer graphene with excellent barrier properties.

Results and discussion

Acid etch of the growth catalyst

The etch test relies on the selective etching of copper in areas underneath defects in CVD graphene to form etch pits when an acid droplet is placed on monolayer graphene grown on copper (see Fig. 1A, S6C†). Since the resulting etch pits can be much larger than the corresponding defects, the etching process effectively amplifies the defects in graphene.[16] The etch pits can be easily imaged with a scanning electron microscope (SEM)[5,26] and quantified for etch pit area/density, thereby providing a basis for qualitative and quantitative comparison across different samples obtained by changing the CVD processing conditions. The method requires little sample preparation and is quick and easy to perform, enabling a facile analysis.

To study the evolution of etch pits with time, we exposed graphene to iron chloride (FeCl$_3$) etch for 5, 30 and 60 s respectively. SEM imaging reveals a clear increase in the size of defects with increasing etch time (Fig. 1B–D), which is also reflected in the etch pit size distribution (Fig. 1E–G). However, with increasing size the coalescence of etch pits leads to a decrease in average etch pit density from 0.0225 to 0.0098 μm^{-2} (Fig. 1H). Similar etch pit densities and increase in the etch pit size are also seen for an etch test with a different etchant, ammonium persulfate (APS, see Fig. S1†), indicating the consistency of the results irrespective of the etchant.

If we hypothesize that etching is limited by mass transport through the graphene defects, then a scaling law relating the etch pit area (observable in SEM) with time should hold. Assuming that the graphene remains intact during the etch test, the dissolved Cu^{2+} ions must exit through the defect as the etch pit grows. If the etch pit is much larger than the defect, for both diffusion-driven and electric field-driven transport, we can expect the rate of efflux of Cu^{2+} to be limited by the defect size, provided that dissolution of copper at the copper/solution interface is not a limiting factor. In the

absence of nonlinear electrokinetic effects, we therefore expect the rate of efflux of Cu^{2+} ions to scale with the defect size R_d. Furthermore, the volumetric rate of growth of the etch pit is directly proportional to the rate of efflux of Cu^{2+} ions. Assuming that the etch pit grows to a size R_c in time t, this simple model predicts the scaling $R_c \propto (R_d t)^{1/3}$ (see Fig. 1I). The model also predicts that the etch pit area should scale as $R_c^2 \propto (R_d t)^{2/3}$. Furthermore, the model predicts only a weak scaling of the etch pit size (R_c) with the defect size (R_d), $R_c \propto (R_d)^{1/3}$, which enables a large range of defect sizes to be probed. This weak scaling is critical to the practical utility of the test by enabling simultaneous analysis of small and large defects in graphene.

The etch pit area, as measured by SEM, indeed shows the expected power law dependence on etch time for both FeCl$_3$ and APS, with exponents of 0.6 and 0.75 respectively, compared to the theoretically predicted exponent of 2/3 (*i.e.*, 0.67) (Fig. 1J). These observations indicate that the scaling law holds, supporting our hypothesis that defects are a limiting factor in the growth of the etch pits, but only as far as the etch pits do not overlap.

However, we also find that there is an uneven distribution of etch pit sizes, so the scaling mechanism is not entirely valid for all defect sizes. Specifically, we find that the etch pit size distribution has two peaks for the FeCl$_3$ etchant, but only a single peak for the APS etchant. Such deviations from the model suggest the involvement of additional mechanisms consistent with differences seen in the etch pit size distribution and coalescence (Fig. 1E–G, S1D–F†) and density (Fig. 1H). We hypothesize that the uneven distribution could arise from the limited potential generated by the etchants *i.e.* the larger pits determine the electric potential of copper, leading to slower growth of smaller pits and suppression of nucleation of pits under small defects, since the etching and potential of copper are influenced by the concentration of Cu^{2+} in solution.[34,35] Taken together, these observations indicate that while the acid etch test is qualitatively useful,[16] caution should be used in applying it as a quantitative metric. Finally, we note from Fig. 1B–D, S1A–C† that the etch pits appear to line up along macroscopic patterns similar to wrinkles typically seen in CVD graphene on Cu.[11]

Electrochemical etch of the growth catalyst

The acid etch test method described above leaves open the possibility that the formation of etch pits underneath very small defects does not occur in the presence of large defects due to insufficient driving potential for their nucleation and growth. To minimize the possibility of such effects, we performed an electrochemical etch test using an externally imposed potential on the graphene-on-copper samples. Such an experiment ensures that the applied potential is available across the entire surface of the sample, which should theoretically allow for the growth of both smaller and larger etch pits underneath smaller and larger defects in graphene, respectively. This test was performed by applying a potential difference across graphene on Cu foil as the cathode and a significantly
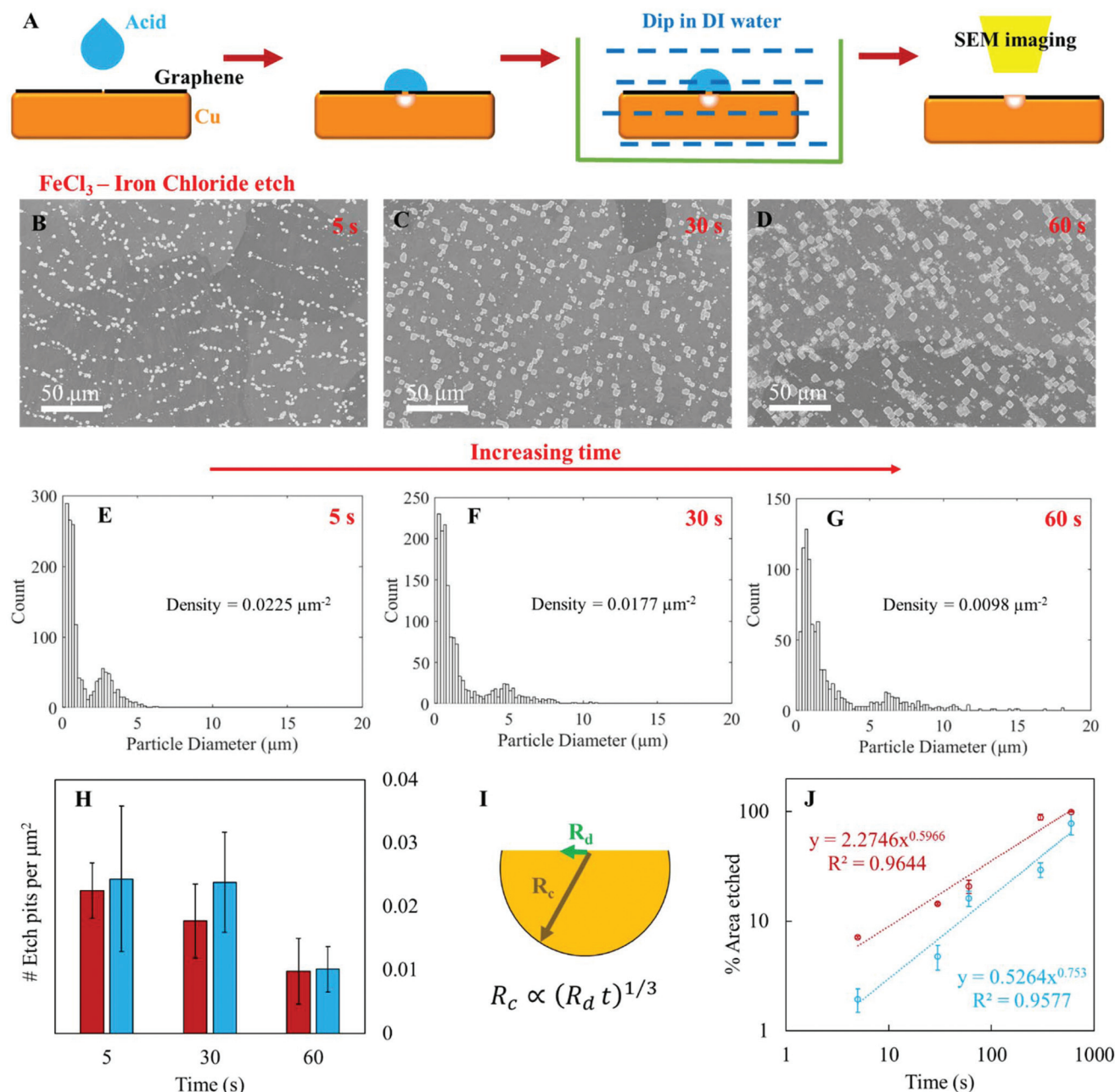
Fig. 1 Acid etch of the growth catalyst as a method to evaluate the quality of graphene for membrane applications and the corresponding scaling model. (A) Schematic illustration of the acid etch process for CVD graphene on Cu foil. SEM images showing the etch pits formed after iron chloride (FeCl$_3$, 0.1 M in water) etch for (B) 5 s, (C) 30 s, (D) 60 s and corresponding size distributions E–G, respectively. The density values are averaged over several representative images. In (B) the etch pits seem to align along features similar to wrinkles seen on graphene on Cu foil. (H) Etch pit density for FeCl$_3$ (red) and APS (blue) as a function of etch time. The density values are averaged over several representative images. Error bars indicate one standard deviation. (I) Scaling model for etch pit formation. (J) % area etched by FeCl$_3$ (red) and APS (blue) as a function of etch time. Error bars indicate one standard deviation.

larger Cu foil as the anode, in 0.5 M copper sulfate solution (see Fig. 2A, B and G). The applied potential difference of 1 V reflects a balance in providing sufficient energy for dissolution of copper, but without causing damage to graphene (see Fig. S2E–G†).[34–38]

To estimate the minimum size of defects in graphene detectable using this method, we use classical nucleation theory to calculate the free energy change involved in creating a new hemispherical etch pit with radius r.

$$\Delta G = -\frac{2}{3}\pi r^3 \Delta g + \pi r^2 \gamma \qquad (1)$$

Where ΔG is the Gibbs free energy involved in the pit formation, Δg is the free energy change for dissolving a unit
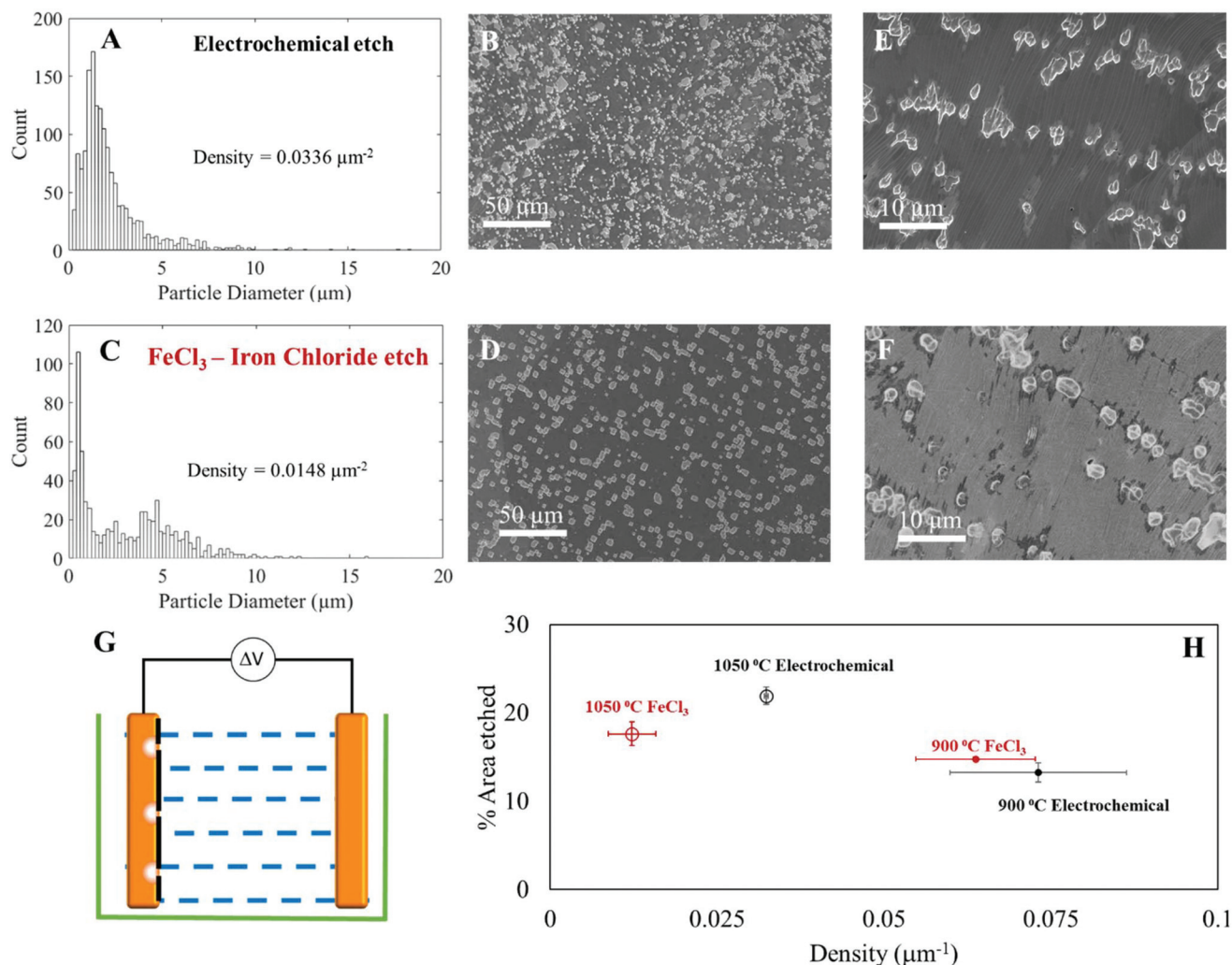
Fig. 2 Electrochemical etch test for controlled driving potential. (A) Size distribution and (B) SEM images for electrochemical etch compared with 30 s FeCl$_3$ etch (C and D) on graphene on Cu. The 1 V, t = 1 s electrochemical etch in 0.5 M CuSO$_4$ solution shows a significantly higher average density of etch pits (∼0.0336 μm^{-2}) compared to FeCl$_3$ (∼0.0148 μm^{-2}). The size of the etch pits is also smaller in the electrochemical etch. (E and F) Show etch pits aligning up along wrinkles in the graphene on Cu for both the electrochemical and acid etch respectively. (G) Schematic of electrochemical etch. (H) % area etched as a function of etch pit density for acid etch with 30 s 0.1 M FeCl$_3$ and electrochemical etch 1 V, t = 1 s for high (∼1050 °C) and low (∼900 °C) quality graphene.

volume of copper, and γ is the Cu/solution surface tension. In an acidic environment of 0.5 M CuSO$_4$ even a potential difference of ∼100 mV readily forms Cu^{2+} from Cu while the potential difference in our experiments is 1 V.[37,38] At equilibrium (0 V applied potential), Δg = 0 and the energy required to create an etch pit is determined by the surface tension. When a potential is applied, the free energy per unit volume $\Delta g = \dfrac{\Delta V n e}{\vartheta}$ favors pit formation on the cathode. Here, ΔV is the applied potential difference, n = 2 is the ion valence, e ∼1.6 × 10^{-19} C is the electron charge, and ϑ ∼1.18 × 10^{-29} m^3 is the atomic volume of Cu. Assuming a surface tension of Cu (∼1.1 N m^{-1})[39,40] as a rough upper bound value of γ and equating the free energy of formation of the etch pit ΔG = 0 gives a critical etch pit size $r_c = \dfrac{0.61 \times 10^{-10}}{\Delta V}$ m. The defect

size in graphene determines the length scale for nucleation of the etch pit, which leads to the result $r_c \approx R_d \approx \dfrac{0.61 \times 10^{-10}}{\Delta V}$ m. Assuming that the potential drop across the graphene-covered Cu is 0.5 V, we calculate r_c = 0.12 nm, which gives a lower bound of ∼0.3 nm for defect sizes in graphene that can be probed with the electrochemical etch. This estimate assumes that the Cu^{2+} concentration in the vicinity of the etch pit is the same as that in a bulk solution, which is not strictly true due to the build-up of Cu^{2+} released from the etched pits. However, the short duration of the etch test (∼1 s) mitigates this effect. Since Cu^{2+} ions must leave through the defect in graphene, the lower bound of detectable defects is practically limited by the size of a hydrated Cu^{2+} ion (∼0.6–0.7 nm).[41]

For comparison, we also performed the acid etch test with FeCl$_3$ on an identical graphene on Cu (see Fig. 2C, D and F,

same CVD growth run and less than 5 mm away from the electrochemical etch sample). The SEM image and corresponding size distributions of etch pits presented in Fig. 2 indeed show a higher etch pit density for electrochemical etch (0.0336 μm^{-2} compared to 0.0148 μm^{-2}) than 30 s acid etch with $FeCl_3$. Furthermore, the etch pit size distribution in the electrochemical etch is unimodal, which indicates that a uniform potential applied to the entire surface of graphene is able to overcome the potential-induced limitations seen in the acid etch test (Fig. 1E–G). Similar observations are also made for graphene grown at a lower temperature ~900 °C (see Fig. S2,† and Fig. 2H). We emphasize that irrespective of the kind of etch used, the etch pits align along wrinkles in CVD graphene on Cu (see Fig. 2E and F).

The quantitative analytical framework developed here is a significant advance over prior qualitative analysis of acid etch methods.[5,16,42] In addition, we find that both $FeCl_3$ and electrochemical etch tests can be performed on samples that are oxidized by exposure to the atmosphere,[43] in contrast to APS that is useful only for newly synthesized samples (see Fig. S3†). Furthermore, the free energy estimates suggest that the electrochemical etch is capable of detecting defects down to ~1 nm in size, below which the defects can present a barrier to the transport of the Cu^{2+} ions. Both tests reveal an interesting co-localization of defects along wrinkles, which we discuss later. The acid etch test is simpler to implement, and given the qualitative similarity between the two tests, we used the acid etch test for screening graphene quality.

Identifying relevant CVD parameters for "barrier/membrane quality graphene"

The ability to easily test the 'impermeability' of synthesized graphene opens the possibility of tuning the graphene synthesis process specifically to improve the 'barrier' quality of graphene. We adapted well-known aspects of graphene growth in the CVD literature,[11,12] in combination with rapid feedback from the etch test, to navigate the large parameter space for CVD of graphene on Cu and identified favorable synthesis conditions for large area 'barrier/membrane quality graphene'.

We initially focused on mitigating relatively large (visible in SEM) defects and holes in graphene. After a typical graphene growth process on Cu, bright particles (most likely SiO_2) which lead to holes in the graphene film[11,44] are observed on the side of the copper foil in contact with the quartz tube (see Fig. S4†). The side facing away from the quartz tube does not contain these particles and is hence used for all the experiments reported here.

Next, we explored the possibility of exploiting the graphene growth mechanism to selectively seal defective regions in monolayer graphene by increasing the carbon chemical potential (by increasing methane flow/supply) to spur the growth of an additional layer of graphene underneath defects. The quality of the resulting graphene was assessed using the acid etch test. The SEM images of CVD graphene on Cu using one- and two-step growth at 1000 °C after acid etch with 0.1 M APS for 10 min (Fig. S5A and B†) show a reduced etch pit density

and etched area for the two-step growth compared to the one-step growth. The one-step growth is comparable to commercially available graphene (see Fig. S6†). For the two-step growth we observe nucleation of the 2nd layer of graphene underneath the 1st layer in contact with the Cu catalyst[45,46] and several such 2nd layer graphene nuclei are seen in close proximity to wrinkles (see Fig. S5C†). We note here that the nucleation of a 2nd layer at the interface between the first graphene layer and the catalyst requires carbon atoms to reach the catalyst surface.[45] We propose that domain boundaries, wrinkles and other defects in the 1st layer offer leakage pathways for the gaseous hydrocarbon to diffuse to the catalyst, dissociate and finally nucleate graphene as shown in the schematic in Fig. S5D.†[11] In particular, the observation of 2nd layer nuclei along wrinkles is consistent with the propensity of etch pits to line up along wrinkles in the etch test, although the reason for this association is unclear since wrinkles are formed during the cooling phase of CVD. Nevertheless, the etch test results indicate that this CVD growth method potentially allows selective plugging of some leakages in the 1st layer by the nucleation of another layer underneath.[45]

Graphene synthesis for membrane and barrier applications requires uniformity over a large area. However, the growth catalysts, i.e. commercially available Cu foils, are inherently polycrystalline with several grain orientations which contribute to different graphene growth properties, and obtaining single crystalline foils in a scalable and cost effective manner remains non-trivial. Here, we use electron back scattered diffraction (EBSD) maps to study the catalyst crystallography after graphene synthesis (Fig. S5E, F and S7†) for electro-deposited and cold rolled foils. We find that cold rolled Cu foils show relatively more uniform grain orientations (majority closer to the 100 plane) over a large area compared to an electro-deposited Cu foil (large proportion closer to the 111 plane but several other orientations are also seen) under the graphene synthesis conditions reported here. We also observe variations in etch pit densities with Cu crystallographic orientations (see Fig. S7F and G†), which suggests that different crystallographic orientations of the Cu catalyst tend to have different levels of defects. We note that we cannot rule out the possibility that this behavior arises due to the differences in the etching rates of different crystallographic orientations. The lack of a reliable method to precisely control the catalyst crystallography during CVD or cost-effective, scalable method to synthesize single crystals of Cu suggests that cold rolled foils that form uniformly oriented grains of Cu are more suitable for graphene synthesis for large area membrane and barrier applications to ensure uniformity in graphene quality.

Having addressed the larger holes, partial sealing of defective regions in graphene and large scale catalyst uniformity, we now focus on the intrinsic crystallographic quality of the individual graphene domains (>20 μm) that form the monolayer. A key parameter in the synthesis of graphene is the temperature of synthesis; a higher temperature is expected to facilitate annealing of defects and enable the synthesis of higher quality graphene, but is limited to ~1050 °C due to melting of Cu

at higher temperatures under low pressure conditions. Fig. S5H and I† show the SEM images of graphene on Cu synthesized using the two-step growth at two different extremes of growth temperatures (900 °C and 1050 °C) after the FeCl₃ etch test for 30 s. The etch test for graphene grown at 900 °C shows a distinctly higher density of etch pits (Fig. S2, S5H† and Fig. 2H) in comparison with graphene grown at 1050 °C (Fig. S5I†). The Raman spectra also show an increased D peak for the graphene grown at 900 °C (Fig. S5G†) compared to graphene grown at 1050 °C, indicating the presence of more defects and dangling bonds. These observations indicate that the temperature of the CVD process is an important parameter that influences the crystallographic quality and defect density in graphene (see Fig. 2H).[11] Here, we note that commercially available graphene, optimized for electronic applications (see Fig. S6B†) also shows a Raman spectrum with a negligible D peak, but with a higher density of etch pits (Fig. S6A and S5A, B†). This illustrates that the acid etch/electrochemical etch tests designed to probe the impermeability of graphene do not necessarily correlate with Raman spectroscopy, and are potentially more relevant to membrane and barrier applications.

Transport measurements across large area atomically thin membranes

To assess whether the etch test accurately reflects the extent to which the graphene is a good barrier to mass transport, we performed transport measurements across the optimized "barrier/membrane quality graphene". For this purpose, we transferred 1 × 1 cm² graphene to a polycarbonate track etch membrane (PCTEM) support with ~200 nm pores (see Fig. 3A). We emphasize that our transfer technique is polymer free, which is crucial to minimize residues on graphene[47] that can negatively influence transport measurements by potentially blocking transport across defects. The SEM images (Fig. 3D–F) of the graphene transferred on to PCTEM show graphene-covered PCTEM pores (dark circular features ~200 nm), wrinkles (yellow arrows), tears introduced during transfer (red arrows) and a small fraction of open PCTEM pores (bright circular features ~200 nm) without graphene. We identify wrinkles as features with a line-like morphology (also see similar features on graphene on Cu[11] see Fig. S5C†) that show slightly higher contrast compared to graphene.[32] Tears appear as either visible holes in the graphene (see Fig. 3F) or bright areas of PCTE (see Fig. 3H–J) which are charged during imaging due to the absence of the conductive graphene on it.

Initially we measure the fraction of PCTEM covered by graphene by comparing the pressure-driven ethanol flow through the PCTEM + graphene and a bare PCTEM membrane using a customized diffusion cell (Fig. 3B). Here, graphene-covered PCTEM pores will offer resistance to ethanol transport while open pores will readily allow transport. A normalized ethanol flux of ~20% (see Fig. 3C, graphene + PCTEM) indicates a graphene coverage of ~80%, in good agreement with the SEM images and typical coverages of 60–80% obtained for direct polymer-free transfer methods.[5]

We then measured diffusion of KCl (K⁺ and Cl⁻ ~0.66 nm) and Allura Red dye (~1 nm) in 0.5 M KCl. Allura Red has two negative charges and is sufficiently large that a defect in graphene that permits its passage will also permit transport of Cu²⁺. Therefore, we expected that the etch test should accurately capture the transport of Allura Red. KCl may pass through defects that are sufficiently small (<1 nm) to present a barrier to Cu²⁺ transport, and hence may or may not agree with the etch test. However, given the propensity of defects in CVD graphene to exhibit a distribution of sizes down to <1 nm with an approximately exponential distribution of defect sizes[5,7] (i.e., with a greater frequency of smaller pores and rare occurrence of larger pores), we expected to see differences in KCl and Allura Red transport in the presence of such defects due to the smaller size of K⁺ and Cl⁻ ions and weaker electrostatic repulsion due to their monovalent charge.[48] Specifically, we compared the diffusive fluxes of KCl and Allura Red as normalized by the flux through PCTEM without graphene.

We find that, for the optimized graphene, the normalized diffusive fluxes measured for KCl (~50%) and Allura Red (~51%) are very similar (Fig. 3C, graphene + PCTEM), indicating the absence of sub-nanometer to nanometer-scale defects (~0.66–4 nm). We emphasize that commercial graphene with the Raman spectrum (Fig. S6B,† negligible D peak) similar to the optimized "membrane/barrier quality graphene" (Fig. S5G,† negligible D peak) shows distinctly different normalized diffusive fluxes for KCl (~62%) and Allura Red (~42%) indicating the presence of sub-nanometer to nanometer sized defects (see Fig. 3C, commercial graphene + PCTEM). We note here that Raman spectroscopy alone is ineffective at capturing quality information for graphene over a large area for membrane and barrier applications.

Although similar normalized fluxes for KCl and Allura Red indicate the absence of sub-nanometer and nanometer-scale pores, it does not rule out the presence of larger defects. However, if graphene were completely defect-free, we would expect the normalized transport rate of a pressure-driven ethanol flow to be equal to the diffusion-driven flow of KCl and Allura Red. Taking into account that (i) diffusive flow scales as D^2/L, (ii) pressure-driven flow rate scales as D^4/L (L is the pore length ~10 μm and D is the pore diameter ~200 nm for a cylindrical PCTEM pore[5]), (iii) the resistance offered by graphene pores to pressure-driven flow scales as D_p^3 (D_p is the pore diameter) and (iv) the diffusion-driven flow across graphene pores scales as D_p, we estimate that graphene defects ~50 nm or ~4 nm would reduce the pressure-driven and diffusion-driven flow, respectively, by half compared to an open PCTEM pore.[24] The discrepancy between normalized pressure and diffusion driven fluxes (see Fig. 3C, graphene + PCTEM) indicates the presence of defects <50 nm that offer different resistances to the diffusive transport and pressure driven flow.

High resolution SEM imaging indeed confirms the presence of such defects (<50 nm, see Fig. 3E and F) seen primarily along wrinkles in the graphene, and consistent with obser-
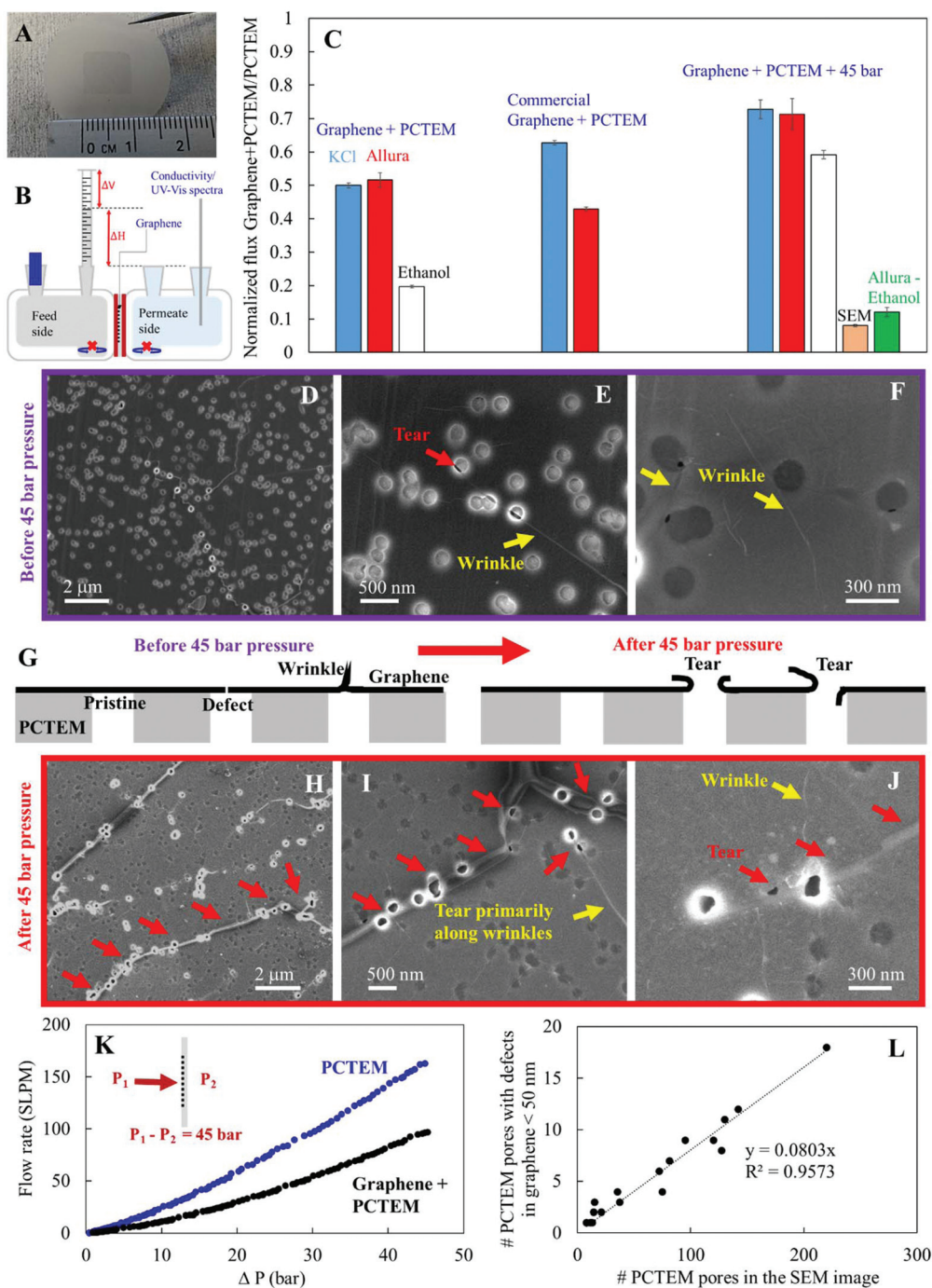
Fig. 3 Pressure differential to selectively damage wrinkles. (A) Optical image of large area graphene transferred onto the polycarbonate track (200 nm pore) etched membrane (PCTEM) support. The dark square at the center is graphene. (B) Schematic of the measurement setup that allows for both pressure driven and diffusion driven flow to be measured on the same membrane area. (C) Flux across graphene + PCTEM normalized by the flux across PCTEM for pressure driven flow with ethanol, diffusion driven flow using KCl and Allura red for graphene + PCTEM before and after 45 bar of pressure differential. Also shown is commercial graphene (Graphenea) + PCTEM for comparison. Error bars indicate one standard deviation. "SEM" denotes the Allura Red flux expected from <50 nm pores enumerated by SEM as shown in (L). "Allura - Ethanol" denotes the difference of normalized fluxes of Allura Red and Ethanol for the Graphene + PCTEM + 45 bar sample. SEM images showing graphene on PCTEM (D–F) before and (H–J) after 45 bar of differential pressure. Red arrows indicate tears in the graphene layer and yellow arrows show wrinkles in the graphene. After differential pressure, tears are primarily seen along wrinkles and the majority of the defects in graphene on PCTEM are converted to tears as shown in the schematic (G). (K) Ar gas flow rate as a function of difference in pressure across PCTEM and PCTEM + graphene. (L) Analysis of SEM images shows PCTEM pores with defects <50 nm as a function of total PCTEM pores in the images. The slope of the line gives the fraction of PCTEM pores covered by graphene that have <50 nm defects which impede pressure driven flow but allow for diffusion driven flow. This fraction (SEM bar) is in good agreement with the difference between the normalized Allura Red or KCl diffusive flux and ethanol pressure driven flux (green bar in C).

vations of etch pits along wrinkles in the etch tests (Fig. 2E and F). To rule out the presence of additional defects other than those associated with wrinkles in graphene (Fig. 3E and F), we subjected another graphene + PCTEM stack to 45 bar argon gas pressure difference (Fig. 3G). This pressure ruptures the graphene primarily along wrinkles to form completely open PCTEM pores (see Fig. 3H and I).[32]

The flow rate as a function of pressure difference for PCTEM and PCTEM + graphene during one such pressure differential experiment shows the graphene-covered PCTEM with a significantly reduced flow compared to the bare PCTEM (Fig. 3K). High-resolution SEM imaging of the graphene + PCTEM stack subjected to 45 bar pressure difference reveals damage to graphene primarily along wrinkles. The majority of the PCTEM pores underneath wrinkles are fully open (Fig. 3H–J), but a small fraction of <50 nm defects are still intact (see Fig. 3I and J). This observation supports the hypothesis that wrinkles are associated with defects and are prone to mechanical failure under stress, including stresses involved in the transfer of graphene from Cu to PCTEM.

The pressure-driven ethanol flux across graphene + PCTEM subjected to 45 bar pressure differential is ~60% (normalized with that across bare PCTEM), while normalized diffusive fluxes for KCl and Allura Red are ~72% and ~71%, respectively (Fig. 3C). To explain this ~11% difference in the ethanol and the Allura Red normalized fluxes, we counted the fraction of <50 nm pores on PCTEM associated with wrinkles that were still intact after the pressure differential (Fig. 3I and J) and plotted the number of PCTEM pores covered by graphene containing sub-50 nm defects, as a function of the total number of PCTEM pores over several SEM images that were analyzed (Fig. 3L). The slope of the linear fit indicates that ~8 ± 0.37% of the PCTEM pores have sub-50 nm defects, in good agreement with the difference of ~11 ± 1.36% between the normalized pressure-driven ethanol flux and diffusion driven Allura Red flux (see Fig. 3C, graphene + PCTEM + 45 bar).

These measurements indicate that sub-50 nm defects primarily seen along wrinkles are indeed the major sources of defects in our CVD graphene optimized for membrane and barrier applications. The probability of additional un-accounted defects in our optimized graphene appears minimal, especially given the low density of defects observed in the electrochemical etch test (~0.0336 μm^{-2}, which translates to 1 defect in graphene over ~950 PCTEM pores $i.e.$, 0.0336 = $1/(950 \times$ area of a PCTE pore in μm^2)) and the close agreement between KCl and Allura Red transport. Furthermore, although the defects along wrinkles may be exacerbated by the graphene transfer process, their presence in the etch test indicates that the defects are formed during CVD synthesis (or after exposure to the atmosphere). A potential reason for the occurrence of defects along wrinkles is the considerable curvature of graphene in the wrinkles, which are formed during the cooling phase of CVD synthesis due to the mismatch of thermal expansion coefficients between graphene and copper.[49,50] The relatively high temperatures when wrinkles may form may lead to rearrangements or defects in the graphene at locations of high curvature. Further studies are required to understand and control these defects.[49,50]

Probing transport across large-area defect-sealed graphene membranes

Having identified the origin of defects in graphene for membrane and barrier applications we returned to the membrane shown in Fig. 3C (graphene + PCTEM). The exact same PCTEM + graphene stack is subjected to interfacial polymerization (IP, see Fig. 4A and B) to selectively seal any large defects or tears in the graphene by forming polymer (nylon 6,6) plugs. This is achieved by the reaction of two monomers (one in the aqueous phase and the other one in the organic phase, see Fig. 4A) only at defect sites in graphene to form a polymer plug.[6] Fig. 4B shows a side view cross-sectional schematic of the IP where the nylon plug is expected to seal the entire PCTEM pore underneath a defect in graphene. Such a defect sealed graphene + PCTEM + IP membrane shows ~49× reduced (or ~98%) diffusion of ~1 nm Allura Red compared to bare PCTEM (Fig. 4C), but allows some transport of KCl. Similar observations of KCl transport are also seen for the control bare PCTEM + IP (Fig. 4C), and hence we attribute the KCl transport to leakage across the nylon 6,6 plugs.

Further, the graphene + PCTEM + IP membranes show ~65× reduction (or ~98.5%) in the He flow rate compared to bare PCTEM (Fig. 4D). To confirm that it is indeed graphene and not IP that is presenting a barrier to transport, we systematically destroyed the graphene + PCTEM + IP membranes with O_2 plasma and measured the pressure-driven He flow rate (Fig. 4E) as a function of plasma exposure. The normalized flow rate of He for the graphene + PCTEM + IP increases at a much higher rate compared to the control PCTEM + IP (only starts increasing beyond 1000 s of plasma exposure), confirming that the barrier and membrane properties are indeed from graphene and that IP is not forming a coating layer over the entire graphene surface. The Raman spectra of graphene subjected to 75 s of O_2 plasma (see the inset in Fig. 4C) confirm damage to graphene with only D and G peaks and the near complete absence of the 2D peak. Further, a clear increase in the normalized diffusion flux of KCl (~80%) and Allura Red (~65%) through the 75 s O_2 plasma treated graphene + PCTEM + IP membranes (Fig. 4C) is also consistent with Raman spectra and He flow rate measurements, thereby confirming that the barrier and membrane properties can be attributed to graphene.

Based on the diffusion measurements presented here, we note that a complete sealing of all pores in PCTEM underneath defects would have resulted in a membrane flux of no more than 50% after destroying all of the graphene (Fig. 4C). While gas measurements confirm the robustness of nylon plugs to O_2 plasma up to at least 300 s (Fig. 4E), an increase in KCl and Allura Red fluxes beyond 50% (Fig. 4C) indicates the possibility that some fractions of the nylon plugs are potentially sealing defects in graphene by forming local plugs selectively at the defects (Fig. 4F and G) as opposed to sealing the entire PCTEM
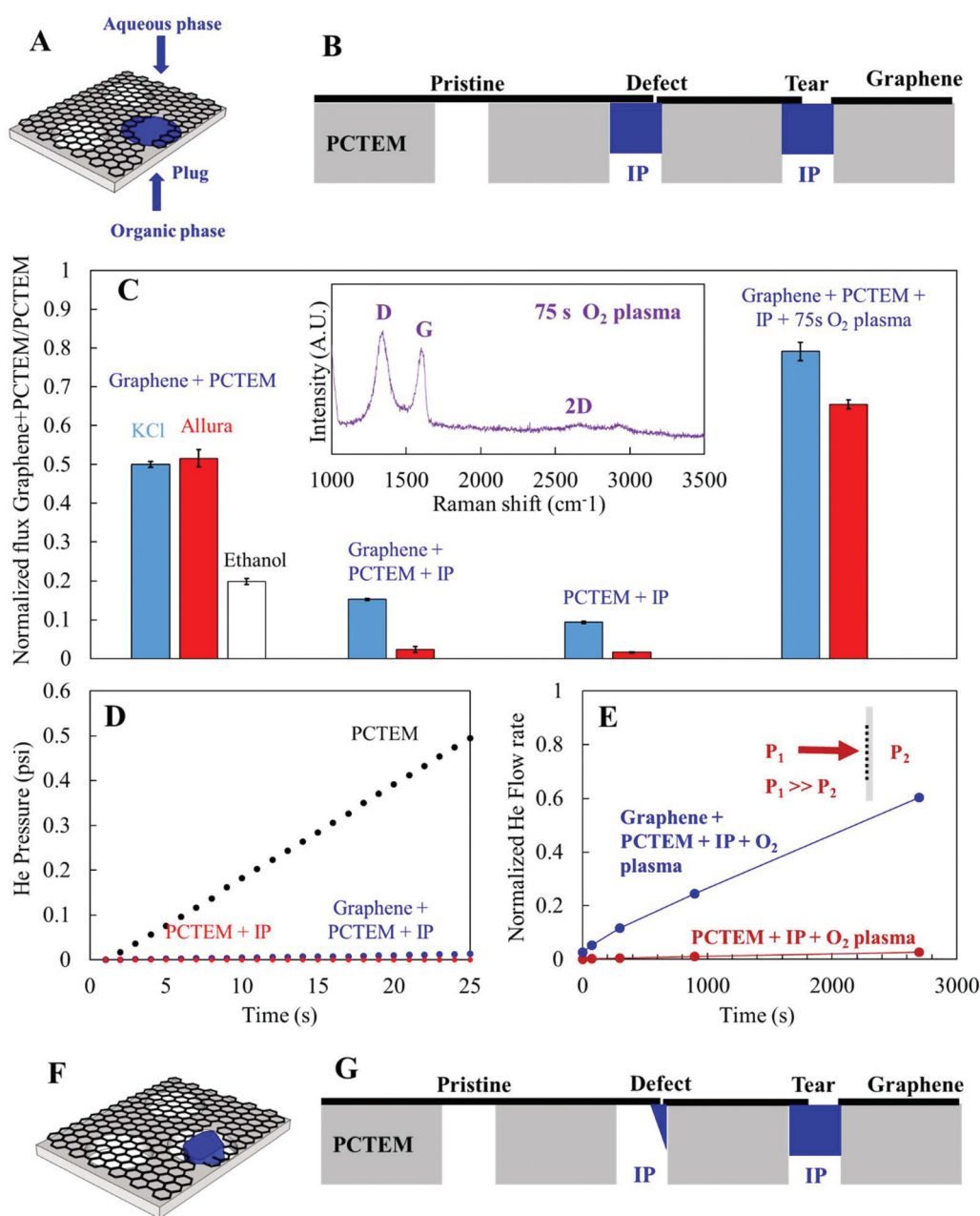
Fig. 4 Probing transport across selective defect-sealed graphene membranes. (A) Schematic of the interfacial polymerization (IP) reaction using an aqueous and organic phase to seal large defects and tears (originating from handling and transfer) in graphene on PCTEM with nylon (6,6) and (B) the principle behind IP formation as reported previously.[6] (C) Flux across graphene + PCTEM normalized by the flux across PCTEM for pressure driven flow with ethanol, diffusion driven flow using KCl and Allura Red for graphene + PCTEM before and after IP, after 75 O_2 plasma post IP and a control PCTEM + IP membrane. Error bars indicate one standard deviation. The inset shows Raman spectra for graphene after 75 s of O_2 plasma. (D) He transport (increase in pressure as a function of time) across PCTEM, graphene + PCTEM + IP and control PCTEM + IP. (E) Normalized pressure driven He flow rate across the graphene + PCTEM membrane after IP and subsequent oxygen plasma etching times. (F and G) Proposed new mechanism of IP formation in the PCTEM supports. Unlike (A and B) the IP forms plugs that locally seal some defects and do not block the entire 200 nm PCTEM pore.

pore (Fig. 4A and B). The formation of local plugs at defect sites renders more area of graphene usable and could potentially be used to seal defects in graphene when suspended over larger areas (current PCTEM pore diameter is ~200 nm) and higher porosity supports (PCTEM support used here has ~10% porosity).

Conclusions

In conclusion, we have shown how a simple etch test can be used to assess the quality of graphene on Cu. The etch test can be used to identify relevant parameters and help navigate the large parameter space for graphene CVD on Cu to tailor the

properties of atomically thin materials for membrane and barrier applications. A combination of the pressure-driven ethanol flow with diffusion-driven KCl and Allura Red flow measurements and high resolution imaging shows that the optimized graphene is devoid of sub-nanometer to nanometer scale defects commonly found in commercial graphene optimized for electronic applications. However, sub-50 nm defects associated with wrinkles remain the main source of defects in CVD graphene for membrane and barrier applications. Finally, using interfacial polymerization to selectively seal these sub-50 nm defects, we demonstrate centimeter-scale atomically thin membranes with ~65× reduction in He flow and membranes with ~49× reduced diffusion of ~1 nm Allura Red compared to bare PCTEM supports. Our work enables the development of a fundamental understanding to tailor the quality of 2D materials and establishes quality metrics for atomically thin gas/liquid separation membranes and ultra-thin barrier materials.

Experimental

Graphene growth

Graphene growth was performed by CVD.[11,12] The Cu foil (25 μm Alfa Aesar 99.8% purity and 18 μm JX Holding 99.9% purity HA, HA-2 and electro-deposited foil) was initially sonicated in 10% HNO_3 for 90 s to remove contaminants and oxides from the Cu surface and subsequently washed with de-ionized water and dried with nitrogen. The Cu foil was loaded into a hot walled tube furnace reactor and annealed at 1050 °C for 60 min in hydrogen at ~1.14 Torr. Graphene growth was performed by adding methane to hydrogen at 900–1050 °C for 30 min at ~1.14 Torr. For a 2 stage growth, at the end of the 1st growth stage, the flow rate of methane was increased by 2× and the growth was continued for 30 min. The foil was quench cooled by opening the furnace at the end of growth. Graphene on the side of the foil away from the quartz tube was used for all experiments.

We also compared the synthesized membrane/barrier quality graphene with state-of-the-art commercially high quality graphene on Cu from Graphenea Inc.

Catalyst etch tests

1 μL drop of 0.1 M iron chloride ($FeCl_3$) or 0.1 M ammonium persulfate (APS) was placed on CVD graphene grown on Cu foil for 5–600 s to form etch pits in Cu by diffusing through defects in the graphene. Electrochemical etch was performed with a 10 mm × 3 mm graphene on Cu as one electrode and 4 cm × 1 cm Cu foil as the other electrode (see Fig. 2G) in 0.5 M $CuSO_4$ solution for 1–3 V and 1–5 s. After, etch the graphene on Cu was washed by dipping in deionized water. The etch pits were subsequently imaged by using a scanning electron microscope (SEM) and quantified for etch pit area/density by manually setting the threshold for each image using ImageJ software. Etch tests were performed within 12 h of graphene synthesis to avoid effects of Cu oxidation by oxygen intercalation and subsequent oxidation (see Fig. S3†),[12,33] which influences the APS

etch test but not the $FeCl_3$ or electrochemical etch tests. Unless explicitly stated, all etch tests reported here were performed on JX Holding 99.9% HA foil with 2 stage growth at 1050 °C.

Graphene transfer and interfacial polymerization

For the polymer-free transfer process, we initially pre-etched the side of the Cu foil that was in contact with the quartz tube during CVD for 5 min in 0.5 M ammonium persulfate solution in water to remove the graphene from it. Polycarbonate track etch membranes (PCTEM) with 10% porosity, 10 μm thickness (Sterlitech non-PVP coated, hydrophobic) and 200 nm vertically aligned cylindrical pores were then pressed against CVD graphene on the Cu (side facing away from the quartz tube) and the Cu was completely etched with ammonium persulfate (0.5 M). Finally, the graphene + PCTEM stack was rinsed multiple times with deionized water followed by isopropanol.[5] Interfacial polymerization was performed using adipoyl chloride in hexane (organic phase) and hexamethylene diamine in water (aqueous phase) as described elsewhere[6] to seal large tears from handling and transfer with nylon 6,6 plugs. The graphene + PCTEM stack was heated at 110 °C for 12 hours to remove water and promote adhesion before interfacial polymerization.

Characterization

A Helios Nanolab Dualbeam 600 was used to obtain the SEM images of graphene on PCTEM (2 kV, 86 pA, 4 mm working distance using immersion mode with an Everhart–Thornley detector) while a Zeiss Supra/Ultra/Ultra Plus was used to image graphene on Cu (2 kV, 4–6 mm working distance using an InLens detector) and perform EBSD measurements (20 kV, 70° tilt, 15 mm working distance, 60 μm aperture using an EBSD detector). Raman spectra were recorded with a Horiba Raman spectrometer with a 532 nm laser.

Liquid and gas transport measurements

Pressure and diffusion driven flow measurements across defects in graphene were performed by placing the graphene-PCTEM stack between two side by side diffusion cells (Permegear Inc., 5 mm orifice, 7 mL volume) as shown in Fig. 3B and rinsed 3 times with ethanol.[5] A hydrostatic head is used to induce a pressure driven flow across the membranes using ethanol (KOPTEC 200 proof ethanol anhydrous) to facilitate wetting of pores and prevent air bubble formation. After ethanol pressure-driven flow measurements the membrane was rinsed for 5 times with deionized water before diffusion-driven flow measurements were performed.

For the diffusion driven flow, 0.5 M KCl in de-ionized water was placed on the feed side and the increase in the conductivity of permeate side de-ionized water was monitored using a conductivity probe (eDAQ – Isopod). The slopes of the curves are taken after a steady flow was established from 600–900 s to compute a normalized flux for KCl. For Allura Red AC (98%, Sigma-Aldrich) diffusion was measured using 1 mM concentration in 0.5 M KCl on the feed side and a UV-Vis spectrometer (Agilent – Cary 60) measured the increase in the concentration of the Allura Red molecules diffusing into a 0.5 M KCl solution on the permeate

side (to rule out electro-kinetic effects). The difference in the UV-Vis spectra between 710 cm^{-1} (deionized water reference) and 510 cm^{-1} (Allura Red peak) was used to compute concentrations. The ratio of the flux across graphene + PCTEM to that of bare PCTEM was used to compute the normalized flux, *i.e.* $\left(\dfrac{\text{flow across graphene + PCTEM}}{\text{flow rate across PCTEM}}\right)$. All measurements were repeated in triplicate and both sides of the cell were vigorously stirred to minimize concentration polarization.

Gas transport measurements were performed using a customized setup as described elsewhere.[7] Here the increase in the pressure of an evacuated chamber was monitored by pressurizing the graphene side of the graphene + PCTEM with He.

Pressure difference to rupture defects on wrinkles in graphene

Pressure difference measurements were performed as reported elsewhere.[32] Briefly, the copper masking tape (TED PELLA 16072-1) was used to cover regions of the PCTEM other than a circular graphene-covered region subjected to measurements. The copper mask + graphene + PCTEM was then placed on a porous metal support.[32] Argon was used as the pressurizing gas to create a pressure difference of 45 bar through a pressure regulating valve downstream (set to ~5 bar). Pressure gauges upstream (~50 bar) and downstream were used to monitor pressure, while a flow meter upstream measured the gas flow.

Author contributions

P. R. K. and R. K. designed the experiments and wrote the manuscript. P. R. K. performed the experiments. R. A. T. helped with image analysis. L. W. performed the high pressure tests. M. S. H. B. performed gas transport measurements. All authors contributed to discussions.

Conflict of interest statement

R. K. discloses financial interest in a company aimed at commercializing graphene membranes.

Acknowledgements

References

1 J. S. Bunch, S. S. Verbridge, J. S. Alden, A. M. Van Der, J. M. Parpia, H. G. Craighead, P. L. Mceuen, J. S. Bunch, S. S. Verbridge, J. S. Alden, A. M. Van Der Zande, J. M. Parpia, H. G. Craighead, P. L. Mceuen, A. M. Van Der Zande, J. M. Parpia, H. G. Craighead and P. L. Mceuen, *Nano Lett.*, 2008, **8**, 2458–2462.

2 R. N. Karnik, *Nature*, 2014, **516**, 173–175.

3 S. Hu, M. Lozada-Hidalgo, F. C. Wang, A. Mishchenko, F. Schedin, R. R. Nair, E. W. Hill, D. W. Boukhvalov, M. I. Katsnelson, R. a. W. Dryfe, I. V. Grigorieva, H. A. Wu and A. K. Geim, *Nature*, 2014, **516**, 227–230.

4 A. K. Geim and K. S. Novoselov, *Nat. Mater.*, 2007, **6**, 183–191.

5 S. C. O'Hern, C. a. Stewart, M. S. H. Boutilier, J. C. Idrobo, S. Bhaviripudi, S. K. Das, J. Kong, T. Laoui, M. Atieh and R. Karnik, *ACS Nano*, 2012, **6**, 10130–10138.

6 S. C. O'Hern, D. Jang, S. Bose, J.-C. Idrobo, Y. Song, T. Laoui, J. Kong and R. Karnik, *Nano Lett.*, 2015, **15**, 3254–3260.

7 M. S. H. Boutilier, C. Sun, S. C. O'Hern, H. Au, N. G. Hadjiconstantinou and R. Karnik, *ACS Nano*, 2014, **8**, 841–849.

8 S. C. O'Hern, M. S. H. Boutilier, J. C. Idrobo, Y. Song, J. Kong, T. Laoui, M. Atieh and R. Karnik, *Nano Lett.*, 2014, **14**, 1234–1241.

9 K. Celebi, J. Buchheim, R. M. Wyss, A. Droudian, P. Gasser, I. Shorubalko, J.-I. Kye, C. Lee and H. G. Park, *Science*, 2014, **344**, 289–292.

10 E. N. Wang and R. Karnik, *Nat. Nanotechnol.*, 2012, **7**, 552–554.

11 P. R. Kidambi, C. Ducati, B. Dlubak, D. Gardiner, R. S. Weatherup, M. Martin, P. Seneor, H. Coles and S. Hofmann, *J. Phys. Chem. C*, 2012, **116**, 22492–22501.

12 P. R. Kidambi, B. C. Bayer, R. Blume, Z.-J. Wang, C. Baehtz, R. S. Weatherup, M.-G. Willinger, R. Schloegl and S. Hofmann, *Nano Lett.*, 2013, **13**, 4769–4778.

13 P. R. Kidambi, R. Blume, J. Kling, J. B. Wagner, C. Baehtz, R. S. Weatherup, R. Schloegl, B. C. Bayer and S. Hofmann, *Chem. Mater.*, 2014, **26**, 6380–6392.

14 S. Bae, H. Kim, Y. Lee, X. F. Xu, J. S. Park, Y. Zheng, J. Balakrishnan, T. Lei, H. R. Kim, Y. I. Song, Y. J. Kim, K. S. Kim, B. Ozyilmaz, J. H. Ahn, B. H. Hong and S. Iijima, *Nat. Nanotechnol.*, 2010, **5**, 574–578.

15 X. Li, W. Cai, J. An, S. Kim, J. Nah, D. Yang, R. Piner, A. Velamakanni, I. Jung, E. Tutuc, S. K. Banerjee, L. Colombo and R. S. Ruoff, *Science*, 2009, **324**, 1312–1314.

16 M. Hofmann, Y. C. Shin, Y. P. Hsieh, M. S. Dresselhaus and J. Kong, *Nano Res.*, 2012, **5**, 504–511.

17 D. L. Duong, G. H. Han, S. M. Lee, F. Gunes, E. S. Kim, S. T. Kim, H. Kim, Q. H. Ta, K. P. So, S. J. Yoon, S. J. Chae, Y. W. Jo, M. H. Park, S. H. Chae, S. C. Lim, J. Y. Choi and Y. H. Lee, *Nature*, 2012, **490**, 235–239.

18 D. W. Kim, Y. H. Kim, H. S. Jeong and H. Jung, *Nat. Nanotechnol.*, 2011, 1–6.

19 A. W. Tsen, L. Brown, M. P. Levendorf, F. Ghahari, P. Y. Huang, R. W. Havener, C. S. Ruiz-Vargas, D. a. Muller, P. Kim and J. Park, *Science*, 2012, **336**, 1143–1146.

20 N. Petrone, C. R. Dean, I. Meric, A. M. van der Zande, P. Y. Huang, L. Wang, D. Muller, K. L. Shepard and J. Hone, *Nano Lett.*, 2012, **12**, 2751–2756.

21 J. Hong, J.-B. Lee, S. Lee, J. Seo, H. Lee, J. Y. Park, J.-H. Ahn, T. Il Seo, T. Lee and H.-B.-R. Lee, *NPG Asia Mater.*, 2016, **8**, e262.

22 S. P. Surwade, S. N. Smirnov, I. V. Vlassiouk, R. R. Unocic, G. M. Veith, S. Dai and S. M. Mahurin, *Nat. Nanotechnol.*, 2015, **10**, 459–464.

23 J. Hong, S. Lee, S. Lee, H. Han, C. Mahata, H.-W. Yeon, B. Koo, S.-I. Kim, T. Nam, K. Byun, B.-W. Min, Y.-W. Kim, H. Kim, Y.-C. Joo and T. Lee, *Nanoscale*, 2014, **6**, 7503–7511.

24 P. R. Kidambi, M. S. H. Boutilier, L. Wang, D. Jang, J. Kim and R. Karnik, *Adv. Mater.*, 2017, 1605896.

25 S. Seethamraju, S. Kumar, K. B. Bharadwaj, G. Madras, S. Raghavan and P. C. Ramamurthy, *ACS Nano*, 2016, **10**, 6501–6509.

26 T. H. Ly, D. L. Duong, Q. H. Ta, F. Yao, Q. A. Vu, H. Y. Jeong, S. H. Chae and Y. H. Lee, *Adv. Funct. Mater.*, 2013, **23**, 5183–5189.

27 F. Guo, G. Silverberg, S. Bowers, S.-P. Kim, D. Datta, V. Shenoy and R. H. Hurt, *Environ. Sci. Technol.*, 2012, **46**, 7717–7724.

28 R. S. Weatherup, L. D'Arsié, A. Cabrero-Vilatela, S. Caneva, R. Blume, J. Robertson, R. Schloegl and S. Hofmann, *J. Am. Chem. Soc.*, 2015, **137**, 14358–14366.

29 B. M. Yoo, H. J. Shin, H. W. Yoon and H. B. Park, *J. Appl. Polym. Sci.*, 2014, **131**, 39628.

30 B. Wang, B. V. Cunning, S.-Y. Park, M. Huang, J.-Y. Kim and R. S. Ruoff, *ACS Nano*, 2016, **10**, 9794–9800.

31 K. Choi, S. Nam, Y. Lee, M. Lee, J. Jang, S. J. Kim, Y. J. Jeong, H. Kim, S. Bae, J.-B. Yoo, S. M. Cho, J.-B. Choi, H. K. Chung, J.-H. Ahn, C. E. Park and B. H. Hong, *ACS Nano*, 2015, **9**, 5818–5824.

32 L. Wang, C. M. Williams, M. S. H. Boutilier, P. R. Kidambi and R. Karnik, *Nano Lett.*, 2017, **17**, 3081–3088.

33 R. Blume, P. R. Kidambi, B. C. Bayer, R. S. Weatherup, Z.-J. Wang, G. Weinberg, M.-G. Willinger, M. Greiner, S. Hofmann, A. Knop-Gericke and R. Schlögl, *Phys. Chem. Chem. Phys.*, 2014, **16**, 25989–26003.

34 M. Georgiadou, *J. Electrochem. Soc.*, 1993, **140**, 1348.

35 C. Bryce and D. Berk, *Ind. Eng. Chem. Res.*, 1995, **34**, 1412–1418.

36 S. Garaj, W. Hubbard, A. Reina, J. Kong, D. Branton and J. a. Golovchenko, *Nature*, 2010, **467**, 190–193.

37 D. Grujicic and B. Pesic, *Electrochim. Acta*, 2002, **47**, 2901–2912.

38 J. M. Steigerwald, *J. Electrochem. Soc.*, 1995, **142**, 2379.

39 H. Udin, *Surface Tension of Solid Copper*, MIT, 1957.

40 K. I. Popov, *J. Serb. Chem. Soc.*, 2002, **67**, 769–775.

41 Q. Wang, X. F. Huang, C. X. Li, L. Q. Pan, Z. H. Wu, T. D. Hu, Z. Jiang, Y. Y. Huang, Z. X. Cao, G. Sun and K. Q. Lu, *AIP Adv.*, 2012, **2**, 22107.

42 Y. Hsieh, M. Hofmann, K. Chang, J. G. Jhu, Y. Li, K. Y. Chen, C. C. Yang, W.-S. Chang and L.-C. Chen, *ACS Nano*, 2014, **8**, 443–448.

43 M. Schriver, W. Regan, W. J. Gannett, A. M. Zaniewski, M. F. Crommie and A. Zettl, *ACS Nano*, 2013, **7**, 5763–5768.

44 A. Ibrahim, S. Akhtar, M. Atieh, R. Karnik and T. Laoui, *Carbon*, 2015, **94**, 369–377.

45 S. Nie, W. Wu, S. Xing, Q. Yu, J. Bao, S. Pei and K. F. McCarty, *New J. Phys.*, 2012, **14**, 93028.

46 Q. Li, H. Chou, J. Zhong, J. Liu, A. Dolocan, J. Zhang, Y. Zhou, R. S. Ruoff, S. Chen and W. Cai, *Nano Lett.*, 2013, **13**, 486–490.

47 R. C. Rollings, A. T. Kuan and J. A. Golovchenko, *Nat. Commun.*, 2016, **7**, 11408.

48 T. Jain, B. C. Rasera, R. J. S. Guerrero, M. S. H. Boutilier, S. C. O'Hern, J.-C. Idrobo and R. Karnik, *Nat. Nanotechnol.*, 2015, **10**, 1053–1057.

49 Y. Zhang, Q. Fu, Y. Cui, R. Mu, L. Jin and X. Bao, *Phys. Chem. Chem. Phys.*, 2013, **15**, 19042–19048.

50 B. Vasić, A. Zurutuza and R. Gajić, *Carbon*, 2016, **102**, 204–310.

51 P. R. Kidambi, D. Jang, J. Idrobo, M. S. Boutilier, L. Wang, J. Kong and R. Karnik, *Adv. Mater.*, DOI: 10.1002/adma.201700277.